

Rapid computation of the amplitude and phase of tightly focused optical fields distorted by scattering particles

Janaka C. Ranasinghesagara,^{1,2} Carole K. Hayakawa,^{1,2} Mitchell A. Davis,³
Andrew K. Dunn,³ Eric O. Potma,^{2,4} and Vasan Venugopalan^{1,2,*}

¹Department of Chemical Engineering and Materials Science, University of California, Irvine, California 92697, USA

²Laser Microbeam and Medical Program, Beckman Laser Institute, University of California, Irvine, California 92697, USA

³Department of Biomedical Engineering, The University of Texas at Austin, Texas 78712, USA

⁴Department of Chemistry, University of California, Irvine, California 92697, USA

*Corresponding author: vvenugop@uci.edu

Received January 14, 2014; revised April 28, 2014; accepted May 7, 2014;
posted May 7, 2014 (Doc. ID 204525); published June 18, 2014

We develop an efficient method for accurately calculating the electric field of tightly focused laser beams in the presence of specific configurations of microscopic scatterers. This Huygens–Fresnel wave-based electric field superposition (HF-WEFS) method computes the amplitude and phase of the scattered electric field in excellent agreement with finite difference time-domain (FDTD) solutions of Maxwell's equations. Our HF-WEFS implementation is 2–4 orders of magnitude faster than the FDTD method and enables systematic investigations of the effects of scatterer size and configuration on the focal field. We demonstrate the power of the new HF-WEFS approach by mapping several metrics of focal field distortion as a function of scatterer position. This analysis shows that the maximum focal field distortion occurs for single scatterers placed below the focal plane with an offset from the optical axis. The HF-WEFS method represents an important first step toward the development of a computational model of laser-scanning microscopy of thick cellular/tissue specimens. © 2014 Optical Society of America

OCIS codes: (170.0180) Microscopy; (260.1960) Diffraction theory; (290.7050) Turbid media.

<http://dx.doi.org/10.1364/JOSAA.31.001520>

1. INTRODUCTION

Advances in laser-scanning microscopy have enabled 3D visualization of molecular composition and structure of thick cellular and tissue samples with submicrometer resolution [1–3]. Despite these successes, several factors limit the image resolution and maximum imaging depth obtained using these techniques [4]. The most prominent amongst these factors is optical scattering, which alters the amplitude and phase of the focused wavefront and results in attenuation, distortion, and depolarization of the focused beam. The spatially heterogeneous nature of scattering in biological tissues is linked directly to their architecture and morphology on spatial scales comparable to the optical wavelength [5,6]. The influence of tissue architecture on the intensity and angular redistribution of scattered light not only compromises imaging depth and resolution, but also limits the ability to obtain quantitative information from the resulting images.

To mitigate the deleterious effects of optical scattering, iterative feedback methods have been developed to correct for resulting wavefront aberrations [7–10]. While such methods are promising, sample heterogeneity demands that wavefront correction be performed at each location within the sample. Such an approach is impractical as it can increase the image acquisition time by orders of magnitude [7,11]. Moreover, these experimental approaches do not advance our fundamental understanding of the relationships between the architecture and composition of biological samples and the resulting focal field distortion. Models that predict focal field distortion for specific configurations of cellular/tissue components would provide important mechanistic insight toward the develop-

ment of strategies to mitigate the negative impacts of light scattering on laser-scanning microscopy.

Unfortunately, existing approaches to model the propagation of tightly focused beams in turbid samples have significant limitations. The finite-difference time-domain (FDTD) method is considered the gold-standard numerical method for solving Maxwell's equations and has been applied to model the focal field distortions produced by cellular components [12]. However, the associated computational cost is enormous as the complete electromagnetic field distributions must be calculated on a voxelized grid that fills the entire computational domain. While the simulation time can be shortened through the use of high-performance computing platforms, the computational costs renders FDTD, as well as other methods such as the discrete dipole approximation method [13] and the discrete particle method [14], impractical for extensive parametric studies.

Conventional Monte Carlo simulations that launch photons from an objective lens and propagate them toward a focal volume have been utilized to model converging laser beams in optical, confocal, and multiphoton microscopy [15–17]. While these models provide qualitative agreement with experimental observations, the locations of photon interactions within the medium are random and fail to provide a mechanistic link between tissue architecture and the resulting wavefront distortions. Hayakawa *et al.* [18,19] advanced the use of Monte Carlo simulations to model focused beam propagation by analyzing the angular dispersion of photon propagation in a turbid medium using Xu's electric field Monte Carlo model [20] in the context of the angular spectrum representation

of diffraction theory [21]. These simulations provided important insights regarding the impact of tissue optical properties and numerical aperture (NA) on the spatial dispersion, attenuation, and depolarization of the focused beam. However, because these approaches do not consider specific scatterer configurations and do not rigorously model diffraction and interference effects, the resulting computations provide a washed out speckle pattern which represents only a mean behavior of the focal field.

While several analytical methods have been derived to calculate the scattered field resulting from plane wave propagation incident on spherical and nonspherical scatterers [22–25], similar derivations for tightly focused beams have so far been limited to a single scatterer placed at a specific location [26–30]. Modeling focal fields in scattering media is challenging because the incident wave propagation possesses strong field gradients and requires full consideration of the three-dimensional field properties. In this work, we introduce a computationally efficient Huygens–Fresnel wave-based electric field superposition (HF-WEFS) method to compute the wavefront distortion produced by the propagation of highly focused laser beams through fixed configurations of multiple scatterers. By contrast, this technique is not limited by the number of scatterers or their locations, and can thus be applied more generally to study scattering of focused beams in turbid media.

We first introduce the HF-WEFS method by detailing the HF decomposition of a focused beam followed by HF plane wave propagation and superposition techniques used in the calculation. We then apply HF-WEFS to model several scatterer configurations and examine the focal field distortions produced by different scatterer sizes and locations. We compare these results to FDTD simulations and comment on the relative strengths of the two approaches. Finally, we perform a parametric study to examine the impact of scatterer size and location on the amplitude and phase distributions of a tightly focused laser beam.

2. METHODS AND THEORY

A. Overview

We consider the case of a monochromatic x -polarized plane wave incident upon an aplanatic lens. We model the lens as aberration-free behaving in accordance with Abbe's sine condition. This allows the lens to be represented geometrically as a spherical reference surface of radius f , where f is the focal length [21]. The angular extent of the reference surface depends on the NA and f . The incident plane wave is refracted by the spherical reference surface and propagates toward the focus as a converging spherical wave. To preserve the properties of electromagnetic wave propagation, we apply the HF principle at the spherical reference surface. According to the HF principle, every point on the spherical reference surface is regarded as a source of HF spherical waves. Each HF spherical wave can be represented by a summation of HF plane wavelets propagating outward from each point [31,32]. In other words, the ensemble of HF plane wavelets propagating in different directions fully represents the HF spherical wave. All HF plane wavelets have the same initial amplitude and phase and their phase advances as they propagate [33].

We consider only the forward propagation of the HF plane wavelets in the forward hemisphere of the HF spherical wave

[34] [Fig. 1(a)]. We determine the locations of origin of each HF spherical wave or radiating point by generating a set of uniformly distributed points on the reference surface while maintaining rotational symmetry [35]. Rather than launching all possible HF plane wavelets from each radiation point source, we use a particle-and-detector-based wavelet tracing technique to improve computational efficiency.

For simulations in a nonscattering medium, each HF plane wavelet directed toward a node in the detector plane is allowed to propagate directly and contribute to the detected electric field, as shown in Fig. 1(a). We calculate the total unscattered electric field through a linear superposition of all partial fields that are generated by HF plane wavelets and arrive at the given detector location. When scatterers are present, we consider each scatterer sequentially and account for all the possible HF plane wavelets that may interact with it, as shown in Fig. 1(b). Each scattering interaction produces a 3D scattered field that can be represented by an ensemble of scattered wavelets. We select the scattered wavelet(s) that would reach a detector node of interest and calculate the electric field contribution(s). This process is continued to determine the partial scattered field generated by each HF plane wavelet. Superposition of all the partial fields at the detector node location provides the total scattered electric field. If more than one scatterer is present, multiple scattering is accounted for by considering the scattered field from the first scatterer as an incident field on a second scatterer and vice versa. It is important to note that for the configurations studied here, the scattered field generated by the first scatterer undergoes considerable geometric attenuation before it becomes incident on the second scatterer. Such an attenuated incident field results in an even weaker scattered field such that the influence of this secondary scattered field on other scatterers is negligibly small. As a result, the contributions of third and higher orders of scattering to the final electric field are negligible, and the results shown here only account for primary and secondary scattering effects.

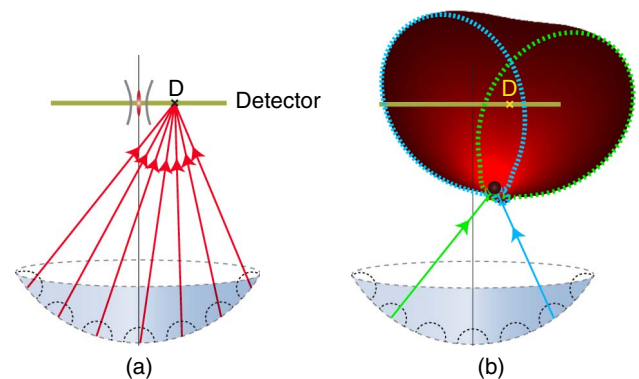


Fig. 1. HF plane wavelets in (a) nonscattering and (b) scattering media. The spherical surface produces a series of forward-propagating HF spherical waves shown as dashed semicircles. In nonscattering media, each HF plane wavelet provides a partial electric field at point D . In media containing scatterers, a HF plane wavelet incident upon a particle produces a complete 3D scattered field. The contribution from each scattered field provides a partial scattered electric field at D . Dashed lines show the boundaries of the scattered field (blue and green). Superposition of two scattered fields gives the total scattered field. Only two HF plane wavelets are shown in (b) for clarity.

B. Theory

A geometrical representation of an aplanatic lens system is provided in Fig. 2(a) [21]. The intensity law of geometrical optics requires that the energy incident on the aplanatic lens is equal to the exiting energy. Thus, in a nonmagnetic medium, the magnitude of the refracted electric field, $|\mathbf{E}(\theta, \phi)|$, can be determined from the magnitude of the incident electric field, $|\mathbf{E}_{\text{inc}}(\theta, \phi)|$, using the following relationship [21]:

$$|\mathbf{E}(\theta, \phi)| = |\mathbf{E}_{\text{inc}}(\theta, \phi)| \sqrt{\frac{n_{\text{inc}}}{n}} (\cos \theta)^{\frac{1}{2}}, \quad (1)$$

where n_{inc} and n are the refractive indices of the medium before and after the lens, respectively, θ is the angle between a refracted wavelet and the optical axis, and ϕ is the azimuthal angle. The origin of the global Cartesian coordinates lies at the nominal focal point. $\mathbf{E}(\theta, \phi)$ can be expressed in terms of the corresponding parallel (E_{\parallel}) and perpendicular (E_{\perp}) components as

$$\mathbf{E}(\theta, \phi) = E_{\parallel} \mathbf{n}_{\theta} + E_{\perp} \mathbf{n}_{\phi}, \quad (2)$$

where \mathbf{n}_{θ} and \mathbf{n}_{ϕ} are unit vectors in the spherical coordinate system [Fig. 2(a)].

We use unit vectors of a local orthonormal coordinate system ($\mathbf{m}, \mathbf{n}, \mathbf{u}$) to track the parallel and perpendicular electric field components in plane wave propagation. \mathbf{m} and \mathbf{n} are unit vectors oriented with the parallel and perpendicular polarization components, respectively, and \mathbf{u} is the unit vector in the direction of wave propagation. Each unit vector in the local coordinate system is defined relative to the global Cartesian coordinate system as $\mathbf{m} = m_x \mathbf{i} + m_y \mathbf{j} + m_z \mathbf{k}$, $\mathbf{n} = n_x \mathbf{i} + n_y \mathbf{j} + n_z \mathbf{k}$ and $\mathbf{u} = u_x \mathbf{i} + u_y \mathbf{j} + u_z \mathbf{k}$. This approach provides ready access to x , y , and z electric field components from the parallel and perpendicular components using

$$\mathbf{E}(r) = \begin{pmatrix} E_x \\ E_y \\ E_z \end{pmatrix} = \begin{pmatrix} m_x & n_x \\ m_y & n_y \\ m_z & n_z \end{pmatrix} \begin{pmatrix} E_{\parallel} \\ E_{\perp} \end{pmatrix}, \quad (3)$$

where $\mathbf{E}(r)$ is the electric field at position $r = (x, y, z)$. We align the initial local coordinates ($\mathbf{m}_0, \mathbf{n}_0, \mathbf{u}_0$) with the unit vectors of the global Cartesian coordinates and apply the following axis transformation to obtain the local coordinate system of a HF plane wavelet ($\mathbf{m}_1, \mathbf{n}_1, \mathbf{u}_1$) radiating from the spherical reference surface [Fig. 2(b)]:

$$\begin{pmatrix} \mathbf{m}_1 \\ \mathbf{n}_1 \\ \mathbf{u}_1 \end{pmatrix} = \begin{pmatrix} \cos \theta \cos \phi & \cos \theta \sin \phi & -\sin \theta \\ -\sin \phi & \cos \phi & 0 \\ \sin \theta \cos \phi & \sin \theta \sin \phi & \cos \theta \end{pmatrix} \begin{pmatrix} \mathbf{m}_0 \\ \mathbf{n}_0 \\ \mathbf{u}_0 \end{pmatrix}, \quad (4)$$

where ϕ and θ are azimuthal and polar angles of the HF plane wavelet with respect to the global coordinate system. The parallel and perpendicular electric field components of the x -polarized beam incident on the lens with $E_{\text{inc}}(\theta, \phi)$ beam profile are equal to $E_{\parallel} = E_{\text{inc}}(\theta, \phi)(1 + i0)$ and $E_{\perp} = E_{\text{inc}}(\theta, \phi)(0 + i0)$, respectively. Combining the attenuation factor in Eq. (1) with the above representation of the incident beam, the electric field components of the HF plane wavelet ($E_{\parallel,1}, E_{\perp,1}$) at the spherical reference surface are given by

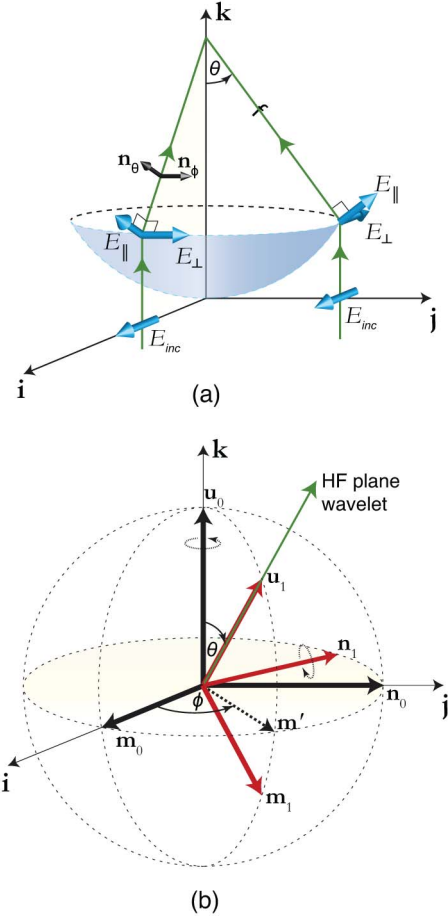


Fig. 2. (a) Geometrical representation of the focused x -polarized flat beam by an aplanatic lens. The x -polarized incident wave (E_{inc}) that is defined by unit vectors \mathbf{i} , \mathbf{j} , and \mathbf{k} is refracted by the reference spherical surface of radius f . E_{\parallel} and E_{\perp} are parallel and perpendicular electric field components after refraction, respectively. (b) The relationship between global and local orthonormal coordinate systems. The initial local coordinate system ($\mathbf{m}_0, \mathbf{n}_0, \mathbf{u}_0$) aligned with the unit vectors of the global Cartesian coordinate system. The local coordinate system for the HF plane wavelet ($\mathbf{m}_1, \mathbf{n}_1, \mathbf{u}_1$) (red) can be calculated by rotating the initial local coordinate system by ϕ and θ , respectively. \mathbf{m}' is the projection of \mathbf{m}_1 on the x - y plane.

$$\begin{pmatrix} E_{\parallel,1} \\ E_{\perp,1} \end{pmatrix} = E_{\text{inc}}(\theta, \phi) \begin{pmatrix} \cos \phi & \sin \phi \\ -\sin \phi & \cos \phi \end{pmatrix} \begin{pmatrix} 1 + i0 \\ 0 + i0 \end{pmatrix} \times \sqrt{\frac{n_{\text{inc}}}{n}} (\cos \theta)^{\frac{1}{2}}. \quad (5)$$

The unscattered electric field components at a distance d from the emitting point are given by

$$\begin{pmatrix} E_{\parallel,1}^{\text{Unscat}} \\ E_{\perp,1}^{\text{Unscat}} \end{pmatrix} = \begin{pmatrix} E_{\parallel,1} \\ E_{\perp,1} \end{pmatrix} \exp(-ikd), \quad (6)$$

where $k = 2\pi/\lambda$ and λ is the wavelength in the medium. In situations where the HF plane wavelet interacts with a scatterer, the local coordinate system is updated by applying an axis transformation using the angles ϕ_s and θ_s similar to Eq. (4) following the scattering event. The angles ϕ_s and θ_s represent the azimuthal and scattering angles of a scattered wavelet relative to the incident HF plane wavelet, respectively. While the outgoing scattered wave radiates in all directions, we consider

only those directions that are directed toward the centers of the other scatterers in the medium and model the relevant scattered wavelets as plane waves incident upon the scatterers.

In this study, we choose to examine spherical scattering particles, for which a full-amplitude scattering matrix for variable particle diameters can be readily obtained from Lorenz–Mie theory [36,37]. We consider a full series expansion of the Lorenz–Mie theory [36] and truncate the series at a sufficiently large value proposed by Bohren and Huffman [37] to achieve an arbitrarily small error. The Lorenz–Mie theory provides the complete scattered field in both near and far fields. In this description, the diagonal amplitude scattering matrix components $S_1(r_s, \theta_s)$ and $S_2(r_s, \theta_s)$ depend on the scattering angle and the distance. We can express the parallel and perpendicular polarization components of the scattered wave for a specific θ_s and distance from the scatterer, r_s as

$$\begin{pmatrix} E_{\parallel}^{\text{Scat}} \\ E_{\perp}^{\text{Scat}} \end{pmatrix} = \frac{1}{kr_s} \begin{pmatrix} S_2(r_s, \theta_s) & 0 \\ 0 & S_1(r_s, \theta_s) \end{pmatrix} \times \begin{pmatrix} \cos \phi_s & \sin \phi_s \\ -\sin \phi_s & \cos \phi_s \end{pmatrix} \begin{pmatrix} E_{\parallel,i} \\ E_{\perp,i} \end{pmatrix}, \quad (7)$$

where $E_{\parallel,i}$ and $E_{\perp,i}$ are the parallel and perpendicular incident electric field components of the i th order of scattering, respectively. The maximum value of i depends on the number of scattering orders considered. It is important to note that the consideration of higher scattering orders increases the computational time. Equation (7) provides the spatial and angular distributions of the scattered field resulting from a plane wave incident upon spherical scatterers. When one scatterer is at distance r_s from another, we apply the Lorenz–Mie theory to obtain $S_1(r_s, \theta_s)$ and $S_2(r_s, \theta_s)$ and calculate the scattered wavelet at distance r_s . This scattered wavelet acts as a plane wave incident upon the other scatterer.

The results of Eqs. (6) and (7) are converted into x , y , and z components using Eq. (3) before superposition. These fields are normalized by the number of HF plane wavelets that are launched from the reference spherical surface to obtain complete unscattered $\mathbf{E}^{\text{Unscat}}(r)$ or scattered $\mathbf{E}^{\text{Scat}}(r)$ electric fields. We calculate the total electric field $\mathbf{E}^{\text{Tot}}(r)$ at any given detector node location r through summation of the scattered and unscattered fields [22,37]

$$\mathbf{E}^{\text{Tot}}(r) = \mathbf{E}^{\text{Scat}}(r) + \mathbf{E}^{\text{Unscat}}(r). \quad (8)$$

C. Simulation Setup

We examine focal field distortions by placing single or multiple spherical scatterers at specific locations proximal to the focal volume. We first examine four cases (A, B, C, D) with different scatterer locations, as shown in Figs. 3(a)–3(d). In case A, the center of the scattering particle is placed 6 μm below the focal plane on the optical axis. Case B considers a particle at the same depth but offset by 2.4 μm left of the optical axis. Case C considers a scattering particle placed 15 μm below the focal plane and offset by 2.4 μm right of the optical axis. Case D considers two particles placed at the positions considered in cases B and C. For case D, which contains two scatterers, we limit our computations to second-order scattering because the contributions of third- and higher-order scattering are negligible. Cases

A–D provide a simple diversity of configurations for the validation of the HF-WEFS method. Finally, in Fig. 3(e) we depict the configuration of parametric studies that consider how particle placement on the x – z plane affects the amplitude and phase of the focal field. These studies consider an array of locations in a rectangular region below the focal plane with a regular grid spacing of 500 nm. In each of these cases we consider particle diameters of 1, 2.5, and 5 μm with a refractive index of 1.377.

In these cases, the lens is embedded in a medium with a refractive index equal to 4/3. This provides $\sqrt{(n/n_{\text{inc}})}$ equal to unity in Eq. (1). We consider a uniform incident beam profile with unit amplitude. The focal length and NA of the lens are 500 μm and 0.667 (in the medium), respectively. $\lambda = 600$ nm is used in the simulations (800 nm light propagating in a medium with a refractive index of 4/3). To determine the emission locations of the HF wavelets from the reference surface, we modify Koay’s code [38] slightly to obtain an axisymmetric, and nearly uniform, distribution of 20,120 points on the reference surface. To evaluate the electric fields following a scattering interaction, we generate and load a lookup table containing the amplitude scattering matrices $S_1(r_s, \theta_s)$ and $S_2(r_s, \theta_s)$ for a fixed set of scattering angles and distances into computer memory prior to running the simulation. These table values are interpolated to determine the S_1 and S_2 values corresponding to the r_s and θ_s values actually encountered during the simulation. We use planar detectors with detector node locations spaced at increments of $\lambda/30$ (20 nm) in the HF-WEFS simulation. The HF-WEFS simulation code was

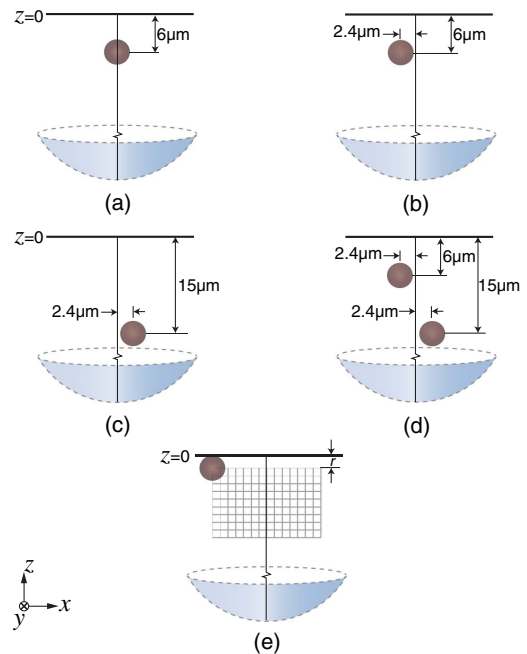


Fig. 3. Schematic of the simulation setup (not to scale). Single scatterers are placed (a) 6 μm below the focal plane for case A, (b) 6 μm below the focal plane and offset by 2.4 μm left of the optical axis for case B, and (c) 15 μm below the focal plane and offset by 2.4 μm right of the optical axis for case C. (d) Case D is a combination of cases B and C. An x – y plane detector is placed at $z = 0$. (e) A single scatterer is placed at different locations in the x – z plane grid ($y = 0$) and its effect on the focal field and the focal volume are considered. The scatterer is placed at the least distance r (radius of the scatterer) below the focal plane and the grid spacing is set to 500 nm. NA and focal length of the lens are 0.667 and 500 μm , respectively.

written in C and simulated on a Windows 7 laptop with an Intel Core i5 M520 2.4 GHz processor and 8 GB RAM memory. No parallel processing is employed.

For comparison, we also simulate electromagnetic wave propagation in cases A–D using a 3D FDTD code. The FDTD implementation uses perfectly matched layer absorbing boundary conditions [39] and a voxel grid spacing of $\lambda/30$ to maintain numerical stability and accuracy. The incident field is computed using the analytical solution of Richards and Wolf [32]. For the FDTD simulations, a parallelized C code was executed on a high-performance computer system at the Texas Advanced Computing Center at the University of Texas at Austin for a volume of $16 \mu\text{m} \times 16 \mu\text{m} \times 40 \mu\text{m}$. The FDTD results are compared directly with the HF-WEFS results without any normalization or scaling.

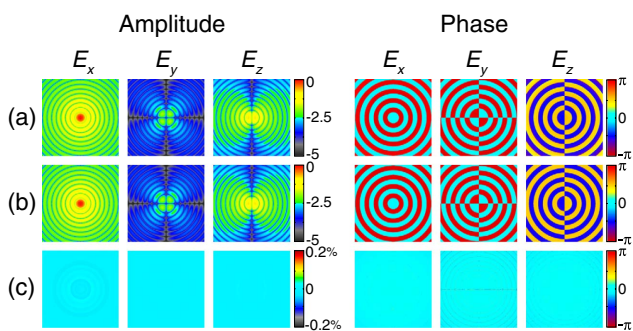


Fig. 4. Unscattered electric field $\mathbf{E}^{\text{Unscat}}(r)$ amplitude and phase at the focal plane predicted using the (a) HF-WEFS method and the (b) Richards and Wolf's analytical solution [32]. (c) The error of the HF-WEFS predictions as a percentage of maximum amplitude of $\mathbf{E}^{\text{Unscat}}(r)$ is shown on the left, and the absolute phase difference is shown on the right. The size of the x - y plane detector is $10 \mu\text{m} \times 10 \mu\text{m}$ with a 20 nm resolution. Amplitude results in (a) and (b) are shown in Log_{10} scale. NA of the lens is 0.667.

3. RESULTS

A. Nonscattering Medium

In Fig. 4, we provide results of HF-WEFS simulations of focused beam propagation in a nonscattering medium. We compare our HF-WEFS computations for the x , y , and z components of the electric field at the focal plane with the analytical solution provided by Richards and Wolf [32]. Each method provides the electric fields at the detector nodes without averaging or interpolation. We calculate the errors through direct subtraction of the analytical solution from the HF-WEFS results. The errors of E_x in the analyzed region are at least three orders of magnitude less than the maximum amplitude of $\mathbf{E}^{\text{Unscat}}(r)$. The results from the HF-WEFS method show excellent agreement with the analytical solution.

B. Scattering Medium: Comparison with FDTD

In Fig. 5, we visualize the focal field resulting from focused beam propagation in the presence of $2.5 \mu\text{m}$ diameter scatterers placed in configurations A–D as predicted by both the HF-WEFS method and FDTD simulations. We plot x , y , and z components of the scattered electric field at the focal plane as predicted by these two techniques. Moreover, the differences in the results are calculated by direct subtraction of the FDTD data from the HF-WEFS computations. The amplitude components of the scattered electric field computed by the HF-WEFS method show good agreement with the FDTD results and all minor features of the field components are preserved. We observe that E_x is the dominant component for x -polarized incident irradiation. The maximum differences of E_x for cases A–D are 1.96%, 3.44%, 4.78%, and 4.75% of the maximum amplitude of $\mathbf{E}^{\text{Scat}}(r)$, respectively. While we observe some limited differences in the predicted E_x and E_z amplitudes as well as the phase of the E_y and E_z components, the absolute amplitude of these differences remains less than 5% of the maximum amplitude of $\mathbf{E}^{\text{Scat}}(r)$. While FDTD computations required 331 processor hours to simulate each single scatterer case (A–C), the HF-WEFS method required only

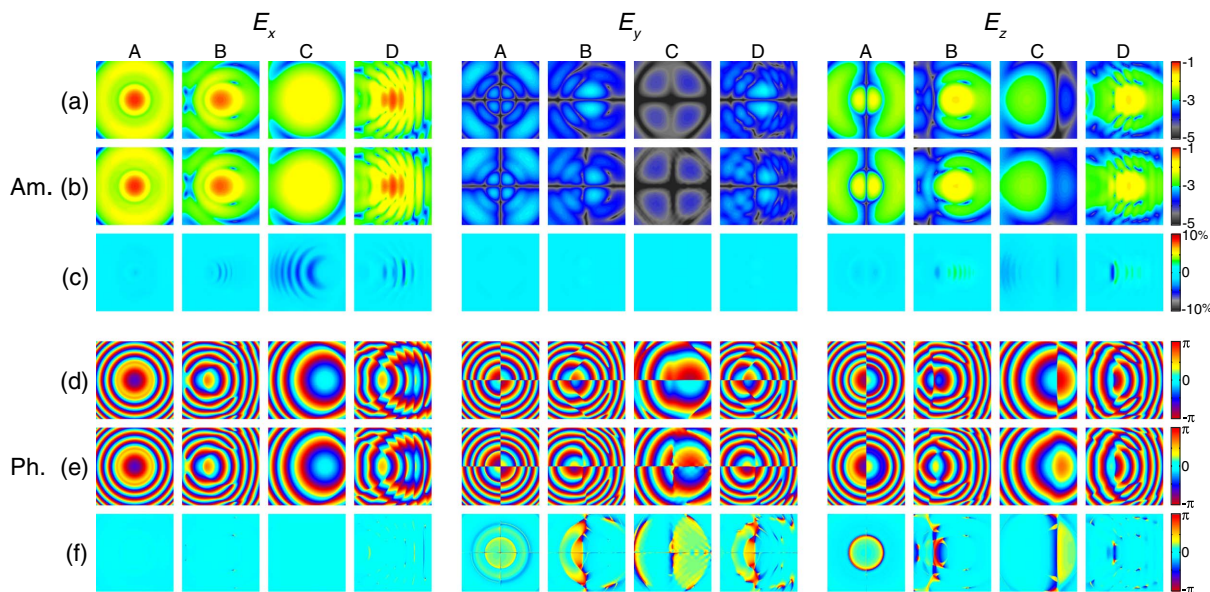


Fig. 5. Scattered electric field $\mathbf{E}^{\text{Scat}}(r)$ at the focal plane predicted using the HF-WEFS method [(a) Amplitude, (d) phase] and the FDTD [(b) Amplitude, (e) phase] for cases A–D. (c) amplitude difference between the methods expressed as the percentage of maximum amplitude of $\mathbf{E}^{\text{Scat}}(r)$. (f) Absolute phase difference. Scatterer diameter is $5 \mu\text{m}$. The size of the x - y plane detector is $10 \mu\text{m} \times 10 \mu\text{m}$ with nodes placed on a square grid with 20 nm spacing. Amplitude results in (a) and (b) are shown in Log_{10} scale. NA of the lens is 0.667.

0.42 processor hours (25 min) for a detector with similar grid spacing.

These results demonstrate that the focal field distortion is influenced greatly by the scatterer size and location. To further examine this behavior, we plot the x - z distribution of the dominant component of the scattered electric field E_x^{Scat} for particle diameters of 1, 2.5, and 5 μm for the four cases A–D at $y = 0$ (Fig. 6). As expected, we observe that larger particles produce higher scattering amplitudes and a highly forward-directed scattered field. The interference of two scattered fields is seen clearly in case D. For scatterers located on the optical axis, the HF plane wavelets that are launched close to the center of the reference surface exhibit a similar propagation phase and their vector summation produces a relatively high scattered amplitude along the z axis. As a result, the amplitudes of the scattered field along the z axis are larger relative to other directions (case A of Fig. 6). For scatterers located off the optical axis, the dominant direction of the incident field on the scatterer depends on the vectorial addition of all HF plane wavelets at the scatterer location (cases B–D in Fig. 6).

C. Metrics for Amplitude and Phase Distortion

The significantly reduced computational costs of the HF-WEFS method as compared to FDTD enables detailed study of the scattering-affected focal volume. To examine the effect of scatterer size and location on the degree of amplitude and phase distortion produced at the focal plane, we place a 4 μm circular detector at the focal plane which is subdivided using a square grid with nodes placed with a 20 nm spacing. The x component of the total electric field $E_x^{Tot}(r)$ is computed at the node locations. In this configuration, we place a single scatterer at different nodes of a grid in the x - z plane, as shown in Fig. 3(e). For each scatterer position, we calculate the 2D amplitude correlation coefficient of the total field with respect to the total field in the nonscattering case. The 2D correlation coefficient is an extension of the Pearson correlation coefficient and assumes values between +1 and -1, where +1 represents perfect correlation and 0 represents no correlation at all [40]. The value of the correlation coefficient for each position of the particle is then plotted as a function of particle position (Fig. 7).

The results for the 1 μm diameter scatterer reveal minimal focal field distortions that are most prominent for scatterer locations proximal to both the optical axis and the focal plane. The scattered field becomes stronger for larger scatterers, which decreases the 2D correlation function. For a 5 μm diameter scatterer, the largest focal field distortions occur for scatterer positions roughly 5 μm below the focal plane and 1.6 μm offset from the optical axis (L_1). When the scatterer is at location L_1 , the scattered field is oblique and highly forward directed (similar to case B in Fig. 6). The constructive interference between the incident and scattered fields produces an asymmetric amplitude profile at the focal plane resulting in very low correlation values. Adjacent to Fig. 7(c), we show that the electric field distribution in the focal field produced by particle position L_2 is more similar to the unscattered case as compared to particle position L_1 . The results reveal not only the prominent effect of particle position on the focal field amplitude but also that the largest field distortions occur for particle positions offset from the optical axis.

In a similar manner, we also consider the 2D correlation coefficients of the detected phase. Figure 8 shows phase correlation maps for 1, 2.5, and 5 μm diameter scatterers. Similar to the amplitude correlations, the phase correlations also decrease for larger scatterers. It is instructive to compare the correlation value for a given scatterer position with the phase distribution detected in the focal plane. These focal plane distributions of the detected phase are shown adjacent to Fig. 8(c) for the 5 μm diameter scatterer. When the 5 μm diameter scatterer is at particle position L_1 , the phases of the scattered and incident fields at the focal plane are not in phase due to the initial phase shift of the scattered field relative to the incident field. As the scattered field amplitude is much larger than the incident amplitude at the focal plane, the phase distribution of the total field is dominated by the phase contribution of the scattered field which results in very low phase correlation values. As the scatterer is moved away from the focal point, the strength of the scattered field decreases and its effect on the detected phase depends on both the amplitude of the scattered field and the relative phases of the incident and scattered fields at the focal plane. If the alignment of these phases at the focal plane are constructive, regardless

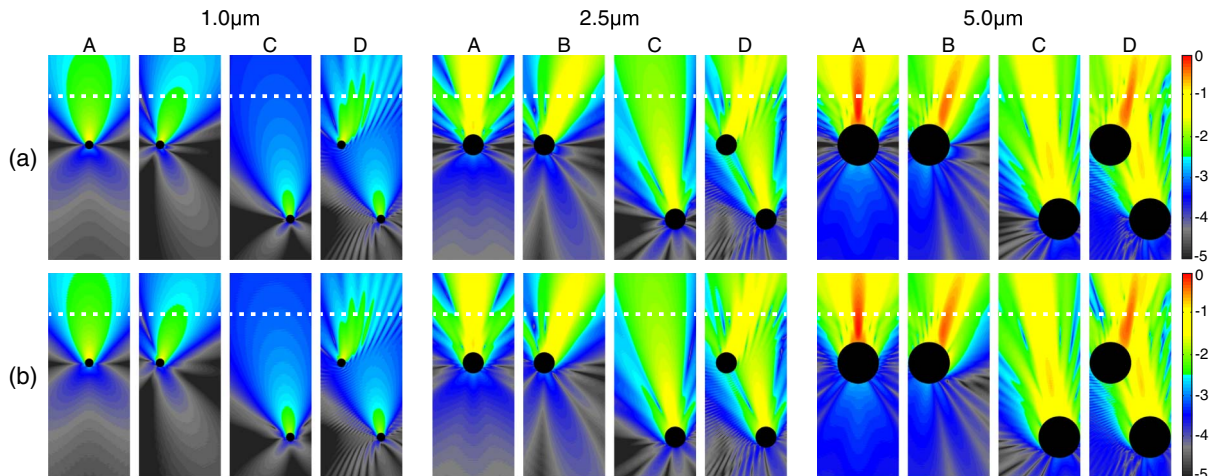


Fig. 6. x component of the scattered electric field amplitude $E_x^{Scat}(r)$ on the x - z plane ($y = 0$) predicted by (a) HF-WEFS and (b) FDTD for cases A–D. Diameters of the scatterers are 1, 2.5, and 5 μm . The horizontal dashed line shows the focal plane. The size of the x - z plane detector is 10 $\mu\text{m} \times 10 \mu\text{m}$ with nodes placed on a rectangular grid with 20 nm spacing. Amplitude results are shown in Log_{10} scale. NA of the lens is 0.667.

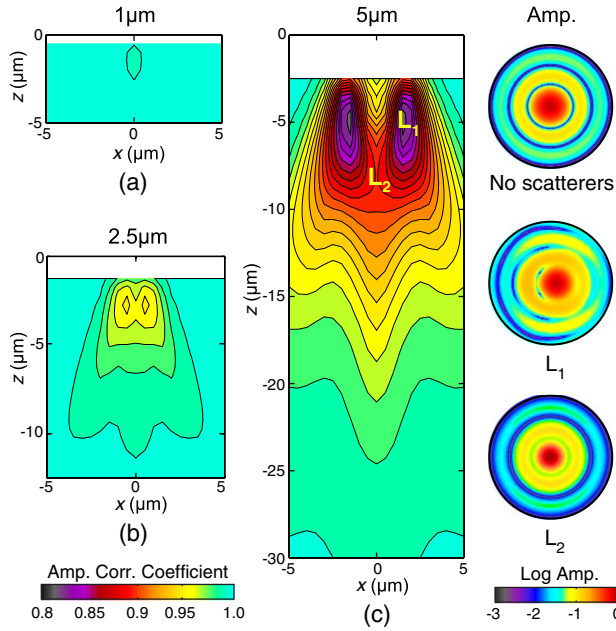


Fig. 7. 2D amplitude correlation coefficient as a function of the x - z particle location of the total x component of the electrical field $E_x^{\text{Tot}}(r)$, as measured on a circular detector placed at the focal plane with respect to the nonscattering case. Scatterer diameters are (a) 1 μm, (b) 2.5 μm, and (c) 5 μm. Contour spacing is 0.01. Right: electric field amplitude distribution profiles in the 4 μm circular detector with nodes placed at 20 nm increments on a square grid for cases with no scatterers, a scatterer positioned at location L₁(-1.6, 0, -5) μm, and a scatterer positioned at location L₂(0, 0, -8) μm in (c).

of the scattered field amplitude, we will observe a high correlation coefficient as in particle position L₂. However, if these phases align destructively and the scattered field amplitude is non-negligible as compared to the incident field amplitude (e.g., in particle position L₄) we will observe a low correlation coefficient. Figure 8 clearly demonstrates the importance of scatterer location on the phase distribution detected in the focal plane.

D. Displacement and Attenuation of Focal Volume

To provide further insight regarding the focal field distortions introduced by a single scatterer, we provide a 3D visualization of the focal field. The 3D visualization is obtained by determining the incident and scattered fields separately and combining all the electric field components to calculate the total electric field $E^{\text{Tot}}(r)$ at each node. Figure 9 shows the total electric field distribution in x - y slices for the nonscattering case and for case B. We observe that the focal volume that is centered around the optical axis in Fig. 9(a) is shifted by 0.2 μm axially and 0.16 μm laterally in Fig. 9(b).

Next, we examine the attenuation and displacement of the focal volume caused by scattering due to their negative impacts on axial and lateral resolution and image registration in biological microscopy. We use the HF-WEFS method to calculate the maximum electric field amplitude and the lateral and axial displacements of the focal volume relative to the nonscattering case. This is accomplished by simulating the electric field distribution of a focused beam in the presence of a single scatterer placed at various locations in the x - z plane and calculating the maximum amplitude and its location

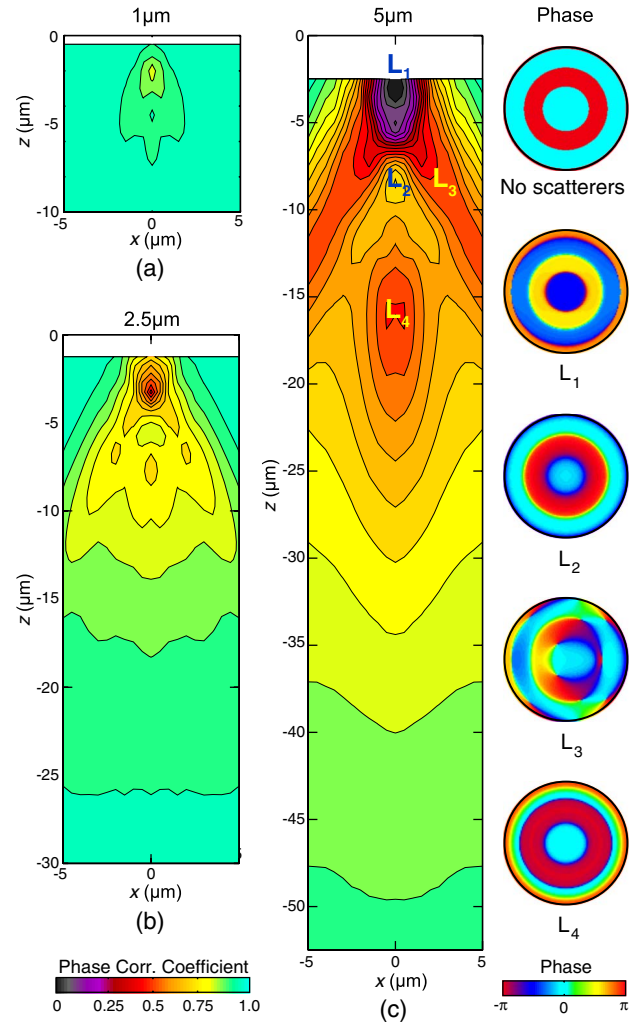


Fig. 8. 2D phase correlation coefficient (E_x^{Tot}) of a circular detector at the focal plane with respect to the nonscattering case is mapped on the x - z plane placement grid. Scatterer diameters are (a) 1 μm, (b) 2.5 μm, and (c) 5 μm. Contour spacing is 0.05. Right: phase distribution profiles in the 4 μm circular detector with nodes placed at 20 nm increments on a square grid for no scatterers, and a scatterer at location L₁(0, 0, -2.5) μm, L₂(0, 0, -8.5) μm, L₃(2.5, 0, -8.5) μm, and L₄(0, 0, -16) μm in (c).

in a 3D detector placed around the focus. In Fig. 10 we show the results for the percentage change in the maximum electric field amplitude in the focal volume relative to the nonscattering case as a function of scatterer location and size. When a scatterer is moved along the optical axis toward the lens, the maximum amplitude in the focal volume displays a bipolar behavior with increases in focal volume amplitude for axial scatterer positions to the focal plane and focal volume amplitude reductions at more distal axial positions [Fig. 10(d)]. The increased amplitude at proximal focal volume positions results from constructive interference of the strong scattered field and nominal incident field, and this effect decreases as the scatterer is moved away from the focal plane.

In Fig. 11 we map the lateral [Figs. 11(a)–11(c)] and axial [Figs. 11(d)–11(f)] displacements of the focal field produced by the placement of a single 1 μm [Figs. 11(a) and 11(d)], 2.5 μm [Figs. 11(b) and 11(e)], and 5 μm [Figs. 11(c) and 11(f)] diameter scatterer in the vicinity of the focal volume. We find that placement of the scatterer along the optical axis results in

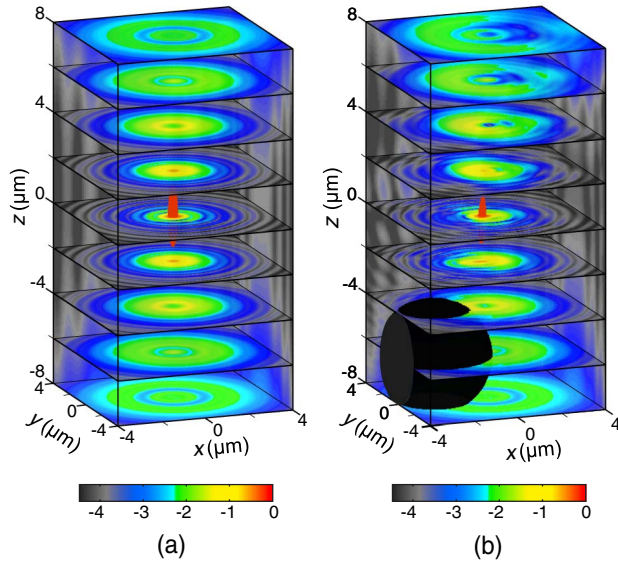


Fig. 9. Total electric field distribution [$E^{\text{Tot}}(r)$] in the focal vicinity (a) for the nonscattering case and (b) by a single scatterer (case B: $5 \mu\text{m}$ diameter). The rendered focal volumes have the same amplitude at the surfaces. Amplitude results are shown in Log_{10} scale.

no lateral displacement of the focal volume. However, for scatterers placed at off-axis locations, strong oblique scattered fields constructively interfere with the incident field that shift the focal volume laterally. The maximum lateral displacement varies with the size and the physical location of the scatterer. When considering axial displacements, introduction of a scatterer in the focal field tends to shift the focal volume toward the lens and shortens the focal length. This trend in axial displacement is clearly shown in the plots presented in Figs. 11(d)–11(f). However, in situations where the scatterer is very close to the focal plane or located in a position that radiates a strong scattered field toward the focus, the focal volume is shifted away from the lens, which gives rise to an extended focal length.

4. DISCUSSION

We have developed a new approach to efficiently model and calculate the amplitude and phase of focused beams in a medium with scatterers placed at specified locations. Application of the Huygens–Fresnel principle at the surface of the spherical reference surface (used to model an aplanatic lens) and propagation of the HF plane wavelets in a nonscattering medium fully preserves the wave diffraction properties of light and provides a diffraction-limited spot at the focal plane. The very small differences ($< 0.1\%$) between the HF-WEFS and the analytical solution shown in Fig. 4 may result from an uneven distribution or finite number of radiating points on the spherical surface. Increasing the quantity and uniformity of the radiation point sources can further minimize these errors at the expense of computational time.

Differences seen between HF-WEFS and FDTD, as shown in Fig. 5, largely depend on the limitations of the FDTD method. In the FDTD computation, both space and time are divided into discrete segments [41] and such an implementation to compute continuously varying electric field amplitudes and phase incurs error. Enlarged x – z plane plots in Fig. 6 clearly demonstrate the discrete nature of the electric

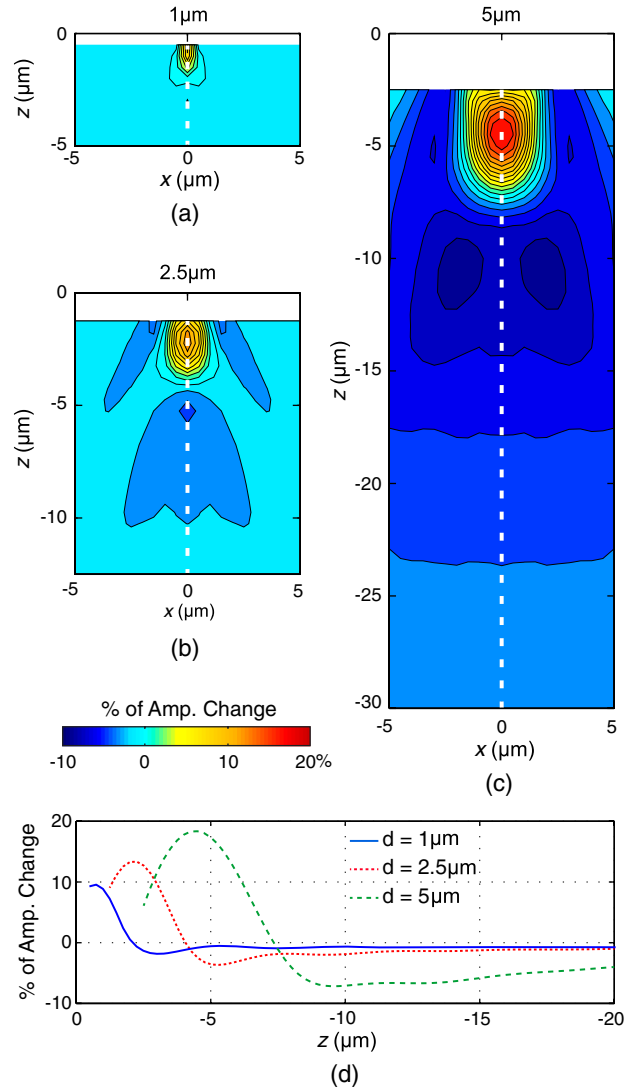


Fig. 10. Percentage change in the maximum electric field amplitude within the focal volume region due to the introduction of a single scatterer with a diameter of (a) $1 \mu\text{m}$, (b) $2.5 \mu\text{m}$, and (c) $5 \mu\text{m}$ as mapped on the x – z placement grid. Contour spacing is 1.5% of the amplitude change. (d) Percentage of amplitude change for a scatterer moving along the optical axis (white dashed line).

field distribution computed by FDTD. It is important to note that in some parts of the FDTD code, single precision floating point arithmetic is used in order to alleviate the high memory requirements while compromising accuracy. Moreover, each spherical scatterer is represented by a composite of cubic voxels which gives rise to a “stair-cased” approximation of the spherical surface. Nonetheless, fine discretization of the FDTD grid at the expense of large memory, storage, and computational cost will minimize differences.

Figures 7–11 show the effects of spherical scatterer size and location on the position and amplitude of the focal volume. Our studies reveal that maximum focal field distortions are not necessarily observed for particles proximal to the focal plane. Instead, maximum focal displacements are observed for scattering objects placed away from the focal plane, while maximum overall change of the focal field amplitude is seen for particle positions offset from the optical axis. These insights may prove indispensable for the further

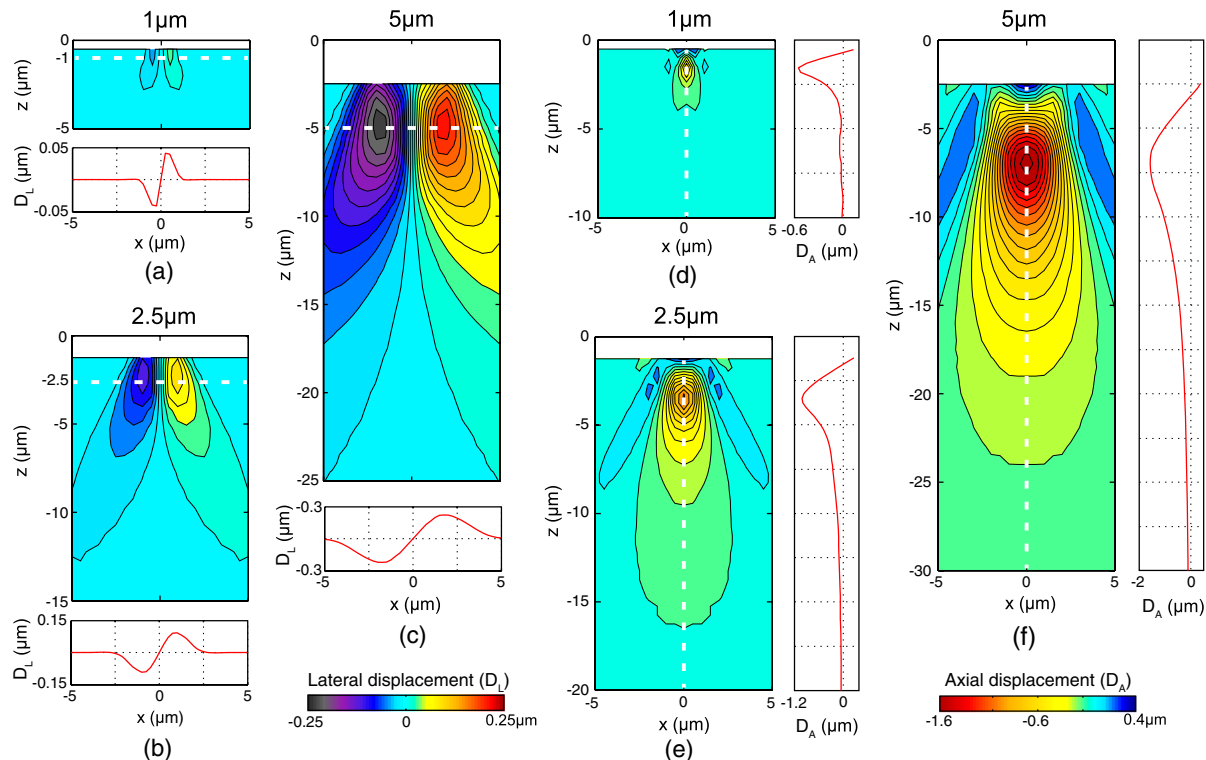


Fig. 11. (a)–(c) Lateral and (d)–(f) axial displacement of the largest amplitude point of the focal volume relative to the nominal focal point due to a single scatterer is mapped on the x – z placement grid. Lateral displacement (D_L) maps with contour spacing of $0.02 \mu\text{m}$ for a single scatterer with a diameter of (a) $1 \mu\text{m}$, (b) $2.5 \mu\text{m}$, and (c) $5 \mu\text{m}$. Axial displacement (D_A) maps with contour spacing of $0.1 \mu\text{m}$ for a single scatterer with a diameter of (a) $1 \mu\text{m}$, (b) $2.5 \mu\text{m}$, and (c) $5 \mu\text{m}$. 1D plots show the displacement profile along the white dashed line.

development of experimental methods to mitigate the effects of scattering for laser-scanning microscopy in thick turbid samples.

The computational cost associated HF-WEFS simulations depends on the number of scattering particles, detector nodes, and HF emission points. The results in Fig. 5 are obtained for an x – y plane detector with 501×501 nodes spanning a $10 \mu\text{m} \times 10 \mu\text{m}$ area. The HF-WEFS simulation time for the single scatterer cases in Fig. 5 is 25 processor minutes which can be reduced by increasing the detector node spacing. While such a change reduces the overall spatial sampling of the focal field, it does not compromise the accuracy of the electric field computed at the detected nodes. For example, by reducing the number of nodes in the detector by 25 times ($\lambda/6$ grid spacing), electric field distributions for the single scatterer cases (Fig. 5) can be obtained in a single processor minute. By contrast, a similar increase in the voxel size in FDTD decreases the simulation time at the expense of reduced accuracy and stability. Without any algorithm optimization or parallel implementation, the HF-WEFS method running on a laptop computer provides a 2–4 orders of magnitude reduction in computational cost as compared to the FDTD method. The significant decrease in computational time relative to FDTD enables extensive parametric studies to gain insight into the effect of scattering size and configuration on focal field distortion. One can improve this advantage further by leveraging multi-core processing capabilities of current processors and faster code optimizing algorithms. The reduced computational time required by the HF-WEFS technique can enable its use to examine wave propagation in turbid slabs, such as those studied using a wave propagation model developed by

Bhargava *et al.* [42]. This would be accomplished by representing each slab with an appropriate number density of scattering particles.

Future studies will focus on the refinement of the HF-WEFS method to compute and analyze focal field distortions produced by specific cellular and tissue components, including organelles, nuclei, and fibrillar structures. This can be realized through simulation of focal field distortions resulting from focused beam propagation through volumes containing multiple particles of complex morphology. The extension of the HF-WEFS method to simulate specific cellular and tissue components can be accomplished using prior knowledge of the amplitude scattering matrix for each scatterer type. For cases where cell or tissue geometries can be approximated by basic geometrical shapes, such as spheres, spheroids, ellipsoids, or cylinders, the amplitude scattering matrix components can be calculated from available sources [43]. We note that the simulation of irregularly shaped scatterers would require larger memory to store amplitude scattering matrix components for each (ϕ, θ) angle pair for each incident direction of the HF wavelets. The use of the HF-WEFS methodology to rigorously model and predict focal fields generated by the propagation of focused beams in scattering media represents the first step toward developing a computationally efficient virtual method to simulate optical microscopy in turbid samples; a capability that currently does not exist. With a prediction of the focal field distribution one can then calculate any number of relevant optical signals, including fluorescence, second-harmonic generation, and/or coherent anti-Stokes–Raman scattering. Emission and propagation of these generated signals from the focal volume can be similarly modeled to better

understand the relationships between the detected emission signal and the tissue characteristics in the focal plane. Hence, the HF-WEFS method brings a practical realization of virtual microscopy in thick turbid samples within reach. This capability has the potential to provide the insights needed to design approaches to improve the qualitative and quantitative information resident in optical microscopy signals obtained from thick biological samples.

5. CONCLUSION

We have introduced the Huygens–Fresnel wave-based electric field superposition (HF-WEFS) method to calculate focal field distortions in scattering media. Implementation of the Huygens–Fresnel principle with phase propagation preserves the wave properties of the tightly focused incident beam and provides accurate focal field predictions in the presence of single or multiple spherical scatterers. This method is several orders of magnitude faster than FDTD and does not require high-performance computer systems to run simulations. We applied the HF-WEFS method to examine the impact of scatterer size and location on the amplitude change and axial/lateral displacements of the focal volume. For single spherical scatterers, we observe maximum focal volume distortions for scatterers placed below the focal plane and, for larger particles, offset from the optical axis. The lower computational cost and scalability of the HF-WEFS method as compared to FDTD methods can enable focal field simulations in even more complicated scattering configurations. Moreover, this rigorous approach to simulate focal field distortions provides an important first step toward the development of a computational framework for modeling laser-scanning microscopy in thick cellular and tissue samples.

ACKNOWLEDGMENTS

JCR, CKH, EOP, and VV acknowledge support from the Laser Microbeam and Medical Program (LAMMP), a NIH Biomedical Technology Resource (P41-EB015890). MAD and AKD acknowledge support from the NIH (R01-EB011556). CKH acknowledges support from the NIH (K25-EB007309). EOP acknowledges support from the NSF (CHE-0847097). MAD acknowledges support from the Consortium Research Fellows Program.

REFERENCES

1. B. A. Wilt, L. D. Burns, E. T. W. Ho, K. K. Ghosh, E. A. Mukamel, and M. J. Schnitzer, "Advances in light microscopy for neuroscience," *Annu. Rev. Neurosci.* **32**, 435–506 (2009).
2. P. Kanchanawong and C. M. Waterman, "Advances in light-based imaging of three-dimensional cellular ultrastructure," *Curr. Opin. Cell Biol.* **24**, 125–133 (2012).
3. E. E. Hoover and J. A. Squier, "Advances in multiphoton microscopy technology," *Nat. Photonics* **7**, 93–101 (2013).
4. R. Heintzmann and G. Ficz, "Breaking the resolution limit in light microscopy," *Briefings Funct. Genomics Proteomics* **5**, 289–301 (2006).
5. A. Dunn and R. Richards-Kortum, "Three-dimensional computation of light scattering from cells," *IEEE J. Quantum Electron.* **2**, 898–905 (1996).
6. J. R. Mourant, T. Fuselier, J. Boyer, T. M. Johnson, and I. J. Bigio, "Predictions and measurements of scattering and absorption over broad wavelength ranges in tissue phantoms," *Appl. Opt.* **36**, 949–957 (1997).
7. Z. Yaqoob, D. Psaltis, M. S. Feld, and C. Yang, "Optical phase conjugation for turbidity suppression in biological samples," *Nat. Photonics* **2**, 110–115 (2008).
8. I. M. Vellekoop, A. Lagendijk, and A. P. Mosk, "Exploiting disorder for perfect focusing," *Nat. Photonics* **4**, 320–322 (2010).
9. T. Čížmár, M. Mazilu, and K. Dholakia, "In situ wavefront correction and its application to micromanipulation," *Nat. Photonics* **4**, 388–394 (2010).
10. S. M. Popoff, A. Aubry, G. Lerosey, M. Fink, A. C. Boccara, and S. Gigan, "Exploiting the time-reversal operator for adaptive optics, selective focusing, and scattering pattern analysis," *Phys. Rev. Lett.* **107**, 263901 (2011).
11. I. M. Vellekoop and A. P. Mosk, "Phase control algorithms for focusing light through turbid media," *Opt. Commun.* **281**, 3071–3080 (2008).
12. M. S. Starosta and A. K. Dunn, "Three-dimensional computation of focused beam propagation through multiple biological cells," *Opt. Express* **17**, 12455–12469 (2009).
13. M. A. Yurkin, A. G. Hoekstra, R. S. Brock, and J. Q. Lu, "Systematic comparison of the discrete dipole approximation and the finite difference time domain method for large dielectric scatterers," *Opt. Express* **15**, 17902–17911 (2007).
14. Z. Cui, Y. Han, and Q. Xu, "Numerical simulation of multiple scattering by random discrete particles illuminated by Gaussian beams," *J. Opt. Soc. Am. A* **28**, 2200–2208 (2011).
15. Z. Song, K. Dong, X. H. Hu, and J. Q. Lu, "Monte Carlo simulation of converging laser beams propagating in biological materials," *Appl. Opt.* **38**, 2944–2949 (1999).
16. X. Deng and M. Gu, "Penetration depth of single-, two-, and three-photon fluorescence microscopic imaging through human cortex structures: Monte Carlo simulation," *Appl. Opt.* **42**, 3321–3329 (2003).
17. A. K. Dunn, V. P. Wallace, M. Coleno, M. W. Berns, and B. J. Tromberg, "Influence of optical properties on two-photon fluorescence imaging in turbid samples," *Appl. Opt.* **39**, 1194–1201 (2000).
18. C. K. Hayakawa, V. Venugopalan, V. V. Krishnamachari, and E. O. Potma, "Amplitude and phase of tightly focused laser beams in turbid media," *Phys. Rev. Lett.* **103**, 43903 (2009).
19. C. K. Hayakawa, E. O. Potma, and V. Venugopalan, "Electric field Monte Carlo simulations of focal field distributions produced by tightly focused laser beams in tissues," *Biomed. Opt. Express* **2**, 278–290 (2011).
20. M. Xu, "Electric field Monte Carlo simulation of polarized light propagation in turbid media," *Opt. Express* **12**, 6530–6539 (2004).
21. L. Novotny and B. Hecht, *Principles of Nano-Optics* (Cambridge University, 2006).
22. D. W. Mackowski, "Analysis of radiative scattering for multiple sphere configurations," *Proc. R. Soc. London Ser. A* **433**, 599–614 (1991).
23. M. I. Mishchenko, J. W. Hovenier, and L. D. Travis, eds., *Light Scattering by Nonspherical Particles: Theory, Measurements, and Applications* (Academic, 2000).
24. H.-X. Xu, "A new method by extending Mie theory to calculate local field in outside/inside of aggregates of arbitrary spheres," *Phys. Lett. A* **312**, 411–419 (2003).
25. F. Borghese, P. Denti, and R. Saija, *Scattering from Model Nonspherical Particles*, 2nd ed. (Springer, 2007).
26. J. P. Barton, D. R. Alexander, and S. A. Schaub, "Internal and near-surface electromagnetic fields for a spherical particle irradiated by a focused laser beam," *J. Appl. Phys.* **64**, 1632–1639 (1988).
27. J. A. Lock, S. Y. Wrbanek, and K. E. Weiland, "Scattering of a tightly focused beam by an optically trapped particle," *Appl. Opt.* **45**, 3634–3645 (2006).
28. J. Lermé, G. Bachelier, P. Billaud, C. Bonnet, M. Broyer, E. Cottancin, S. Marhaba, and M. Pellarin, "Optical response of a single spherical particle in a tightly focused light beam: application to the spatial modulation spectroscopy technique," *J. Opt. Soc. Am. A* **25**, 493–514 (2008).
29. T. X. Hoang, X. Chen, and C. J. R. Sheppard, "Interpretation of the scattering mechanism for particles in a focused beam," *Phys. Rev. A* **86**, 033817 (2012).

30. Y. Jiang, Y. Shao, X. Qu, J. Ou, and H. Hua, "Scattering of a focused Laguerre–Gaussian beam by a spheroidal particle," *J. Opt.* **14**, 125709 (2012).
31. E. Wolf, "Electromagnetic diffraction in optical systems. I. An integral representation of the image field," *Proc. R. Soc. London Ser. A* **253**, 349–357 (1959).
32. B. Richards and E. Wolf, "Electromagnetic diffraction in optical systems. II. Structure of the image field in an aplanatic system," *Proc. R. Soc. London Ser. A* **253**, 358–379 (1959).
33. I. R. Çapoğlu, A. Taflove, and V. Backman, "Generation of an incident focused light pulse in FDTD," *Opt. Express* **16**, 19208–19220 (2008).
34. S. A. Prahl, D. D. Duncan, and D. G. Fischer, "Stochastic Huygens and partial coherence propagation through thin tissues," *Proc. SPIE* **7573**, 75730D (2010).
35. C. G. Koay, "A simple scheme for generating nearly uniform distribution of antipodally symmetric points on the unit sphere," *J. Comput. Sci.* **2**, 377–381 (2011).
36. H. C. van de Hulst, *Light Scattering by Small Particles* (Wiley, 1957).
37. C. F. Bohren and D. R. Huffman, *Absorption and Scattering of Light by Small Particles* (Wiley, 1983).
38. C. G. Koay, "Highly specific but edgily effective data processing (HI-SPEED) software packets," 2014, <https://sites.google.com/site/hispeedpackets/Home/antipodallysymmetricpointset/>.
39. J. P. Berenger, "Three-dimensional perfectly matched layer for the absorption of electromagnetic waves," *J. Comput. Phys.* **127**, 363–379 (1996).
40. E. K. Yen and R. G. Johnston, "The ineffectiveness of the correlation coefficient for image comparisons," research paper (Los Alamos National Laboratory, Los Alamos, New Mexico, 1996).
41. K. S. Yee, "Numerical solution of initial boundary value problems involving Maxwells equations in isotropic media," *IEEE Trans. Antennas Propag.* **14**, 302–307 (1966).
42. B. J. Davis, P. S. Carney, and R. Bhargava, "Theory of midinfrared absorption microspectroscopy: I. Homogeneous samples," *Anal. Chem.* **82**, 3474–3486 (2010).
43. SCATTPORT, "Light scattering Software," 2014, <http://www.scattport.org/index.php/light-scattering-software/>.